

# Chapter 2

## Laser-Based Optical Methods for the Sensory Ecology of Flow Sensing: From Classical PIV to Micro-PIV and Beyond

Thomas Steinmann and Jérôme Casas

**Abstract** This chapter presents an overview of techniques for laser-based, non-contact fluid flow measurements, and their application to real datasets. Particular consideration is given to particle image velocimetry (PIV)-techniques, from the usual macro-scale PIV, through meso-scale PIV, to micro-PIV, thereby spanning the range from decimeter to micrometer scales. We compare the advantages and limitations of these techniques. The specific requirements of sensory ecology and sensory physiology, as well as the 3D-morphological nature of the organisms studied led us to conclude that the techniques that are used in water are ill-suited for several key tasks when dealing with terrestrial organisms. We therefore propose an innovative mixed technology that exploits the advantages of both standard and micro-PIV techniques while avoiding their main limitations.

**Keywords** Particle image velocimetry, micro-PIV • Viscous boundary layer • Filiform hairs • Mechanoreceptors • Sensory ecology • Biomimetics • Flow sensing

### 2.1 Introduction

Flow sensing is used by a vast number of animals (see for example, the reviews of Casas and Dangles (2010) on insects, Engelmann et al. (2002) on fishes, Barth et al. (1993) on arachnids, Denissenko et al. (2007) on crustaceans, Sterbing-D'Angelo et al. (2011) on bats and Hanke et al. (2012) on seals).

---

T. Steinmann (✉) · J. Casas

Faculté des Sciences et Techniques, Institut de Recherche sur la Biologie de l'Insecte, IRBI  
UMR 7261 CNRS, Avenue Monge, Parc Grandmont 37200 Tours, France  
e-mail: thomas.steinmann@univ-tours.fr

J. Casas

e-mail: jerome.casas@univ-tours.fr

The ecological contexts in which flow sensing is relevant are varied: from prey–predator interactions to mate selection, and orientation to flow itself as illustrated in the works cited above. Flow sensing is used in air, water and most likely also in sand and hence in soil (Casas and Dangles 2010; Fertin and Casas 2006, 2007). Flow sensing is one of the several senses used by animals during orientation, and in some cases it is the dominant sense, for example for cave fishes (Windsor et al. 2010a, b). Thus, the study of flow sensing is a vibrant field of research for sensory ecologists and neuroethologists, and also for technologists working on biomimetic sensor design (Casas et al. 2013).

Studies on flow sensing, particularly those at small scale around single sensors, require high spatial precision and nonintrusive measurement methods. Thus, noncontacting measurement methods such as Laser Doppler Anemometry (LDA), Laser Doppler Vibrometry (LDV), and Particle Image Velocimetry (PIV), originally developed by aerodynamics and fluid mechanics engineers, have been used to measure flows of biological relevance. This chapter aims to describe recent technological advances in the measurement of flow around biological and artificial flow sensors in the context of organismal sensory ecology. We start with a description of the state of the art of the various techniques used for flow measurement at the scale of an organism or a sensing organ. We then describe two innovative techniques we have developed for greater spatial resolution, down to the single sensory hair: the first is relatively similar to the standard PIV technique as the particles in the fluid are illuminated by a thin light sheet; the second, micro-PIV, is relatively new to organismal biologists. It is, however, well known to microfluidic engineers, and is based on volumetric illumination. We compare the advantages and limitations of both techniques. In each case, we illustrate our reasoning with a figure or an example. Comprehensive considerations of parameter variations and extended theoretical development can be found in the references provided. The specific requirements of sensory ecology and sensory physiology, combined with the morphological nature of the organisms studied, led us to conclude that both techniques are ill-suited for several key questions. We therefore propose an innovative mixed technology that exploits the advantages of both standard and micro-PIV techniques and avoids their main limitations.

## 2.2 Classical PIV at the Scale of Bodies and Organs ( $10^{-2}$ m– $10^{-3}$ m Resolution)

Due to their improved accessibility, laser-based measurement techniques that were originally restricted to applications in engineering and fluid mechanics are now also used in the fields of locomotion and sensory ecology. In particular, fish physiologists discovered the potential of these techniques to describe complex, unsteady, whole-field flows around an animal's body.

For instance, Bleckmann et al. (1991) used LDA to determine the spectral distribution of hydrodynamic flow fields caused by moving fish, frogs, and crustaceans, and discussed the possible biological relevance of the ability to detect high-frequency hydrodynamic events. Blickhan et al. (1992) used automatic particle tracking and LDA to show that the flow in the wake of a subundulatory swimmer consists of a chain of slightly deformed vortex rings. Two-dimensional PIV was used by Müller et al. (1997) to qualitatively and quantitatively analyze the structure of the wake behind a continuously swimming mullet. More recently, also using PIV, Hanke et al. (2000) found that the wake behind a swimming goldfish can show a vortex structure for at least 30 s. These authors discuss the possible advantage for piscivorous predators of being able to detect and analyze fish-generated wakes. In 2002, Engelmann and colleagues adapted the classical PIV technique for the visualization of the flow around a whole body covered by sensory organs to understand the influence of viscous hydrodynamics on the fish lateral line system (Engelmann et al. 2002).

Chagnaud et al. (2006) analyzed the correlation between neural responses to vortex rings and PIV data. Their artificially generated vortex rings resembled hydrodynamic stimuli that fish might encounter in their natural environments. Denissenko et al. (2007) shed some light on how a hydrodynamic stimulus can be affected by body shape by studying the flow generated by the active olfactory system of the red swamp crayfish. These animals use their anterior fan organs to generate distinct flow patterns that can be used for odor acquisition. The application of PIV to mapping biogenic and biologically relevant flows has been reviewed by Stamhuis et al. (2002).

Catton et al. (2007) quantified the flow fields generated by tethered and free swimming copepods. They report that the area in which the flow velocity was high enough to induce an escape response was 11 times the area of the organism's exoskeletal form. Thus, mechanoreceptive predators may be able to perceive a signal that is spatially extended well beyond the body size (Catton et al. 2007). Windsor et al. (2010a, b), studied the flow field involved in hydrodynamic imaging by blind Mexican cave fishes in open water, both when heading towards a wall and when gliding parallel to a wall. They suggested that the nature of the flow fields surrounding a fish is such that hydrodynamic imaging can be used by fish to detect surfaces at short range.

Wolf spiders live on the surface of leaf litter in forests, where they pursue their cricket prey using two different strategies. Casas et al. (2008) showed, using PIV, that these running spiders are, however, aerodynamically highly conspicuous due to substantial air displacement detectable up to several centimeters in front of them. The airflow in front of running spiders is thus a source of information for escaping prey, such as crickets and cockroaches. More recently, Klopsch et al. (2012) adapted PIV techniques to the study of the flow produced by a fly and sensed by a spider. Their findings led them to propose that the differences in the time of arrival and intensity of the fly signals at their different legs inform spiders about the direction of their prey.

### 2.2.1 Airflow Over a Cricket Body

The cricket *Nemobius sylvestris* uses hundreds of filiform hairs on two cerci as an early warning system to detect remote potential predators. The direction of the attacking predator can be estimated by arrays of hairs that have different directionalities (Landolfi and Jacobs 1995). However, the correct estimation of the direction of the incoming flow field can be biased by the flow perturbation around the cricket's body as a whole. We used PIV to investigate this flow. This technique is mainly used in experimental fluid mechanics to obtain time-resolved velocity measurements and related properties in fluids. The fluid is seeded with tracer particles which are assumed to follow the flow dynamics, and thus the motion of these seeding particles can be used to calculate the velocity of the flow. We will not describe this technique any further, as many books on this topic are available (Raffel et al. 1998; Adrian and Westerweel 2011).

Living crickets were placed in a glass container, with a single loudspeaker producing an oscillatory flow. The air inside the sealed glass box was seeded with 0.2  $\mu\text{m}$  oil particles (Di-Ethyl-Hexyl-Sebacat) using an aerosol generator. The laser of the PIV system illuminated the airflow within the box. The laser sheet (width = 17 mm, thickness = 1 mm) was operated at low power (3 mJ at 532 nm) to minimize glare. A target area was then imaged onto the CCD array of a digital camera (696  $\times$  512 pixels) using a lens (Macro-Nikkon 60 mm). The use of a macro lens allows us to obtain a ratio of the subject plane on the sensor plane of 1:1. Measurements were conducted at 25  $^{\circ}\text{C}$ , corresponding to an air kinematic viscosity of  $\nu_{\text{air}} = 1.59 \times 10^{-5} \text{ m}^2 \text{ s}^{-1}$ . The far-field velocity was set to 10 cm/s and the flow frequency was 80 Hz. We used a stroboscopic principle to sample high frequency oscillatory flow signals with a PIV system limited to 20 Hz (Steinmann et al. 2006). We present here the results for an oscillatory flow parallel to the plane defined by the two cerci; the midline along the cricket abdomen was fixed at an angle of 0 $^{\circ}$  to the direction of the flow.

We found that the orientation of the flow on the surface of a cercus differs from the orientation of the free field flow, i.e. the direction of an incoming flow around the two cerci is strongly altered, as illustrated by the streamlines in Fig. 2.1 (left). The directionality of each of the hairs on the two cerci is crucial as the incoming flow from different directions will trigger different patterns of activity across the whole cercal system (Miller et al. 2011). The projection of each hair into the central nervous system forms a functional map of the current air direction that translates the origin of the incoming flow as three-dimensional spatio-temporal activity patterns (Jacobs et al. 2008). Specifically, the flow direction is slightly shifted counter clockwise on the left cercus and clockwise on the right cercus, i.e. in opposite directions. This has important consequences for the overall computation of the direction of the incoming perturbation as these two effects might cancel each other.

We also observed that the flow amplitude was substantially lower close to the surface of the abdomen than further away (Fig. 2.1, right). The presence of the two

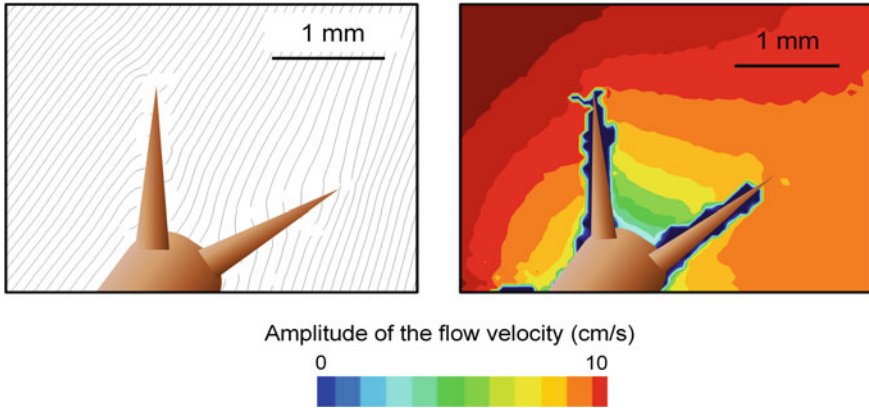


**Fig. 2.1** Flow field around the rear of the wood cricket *Nemobius sylvestris*. On the *left*, streamlines represent the direction of airflow around the cricket's abdomen and cerci. The amplitude of the oscillatory flow in a cross section of the cricket's rear is shown on the *right*

cerci tends to decrease the amplitude of the flow field further, such that flow velocity at the bases of the cerci is considerably reduced. We can therefore conclude that there are substantial differences in the amount of energy available to the different hairs along a cercus.

In many cases, the intrinsic mechanical and neurophysiological properties of a sensory system reflect adaptation to ecologically relevant stimuli. We have illustrated how these stimuli can be greatly modified by the presence of the structure supporting the sensory organs. In addition to the cercus, which functions as a complex filter, the boundary layer over the body has significant implications for the ability of sensory organs to sense stimuli. Our findings agree with previous work with fish (Mc Henry et al. 2008) and crickets (Dangles et al. 2008). Thus, a complete understanding of the performance of a sensory system requires not only a knowledge of all the structural properties of the individual sensory elements but also the determination of the physical environment with exact quantification of the forces that drive these individual receptors.

### 2.2.2 *Structure of Acoustic Flow and Inter-Antennal Velocity Differences in Drosophila melanogaster*

The fruit fly *Drosophila melanogaster* has bilateral antennae of antisymmetric sensitivity. The arista, as well as the funiculus, two parts of the antenna, rotate about a central axis in response to acoustic stimuli. Acoustic communication is important during courtship, and takes place in the acoustic near field, where the small size of the dipole sound source (the male wing) and the rapid attenuation rate of particle velocity are expected to produce a highly divergent and localized sound

field. The small size of the male wing (considered as a dipole sound source) and the rapid attenuation rate of particle velocity produce a spatially divergent sound field of highly variable magnitude. Also, male and female *D. melanogaster* are not usually stationary during courtship, resulting in a variable directionality of the acoustic stimulus (Morley et al. 2012).

Using PIV, we examined the stimulus flow around the head of *Drosophila melanogaster* to identify the true geometry of the acoustic input into the antennae and its directional response. We found that the stimulus changes in both magnitude and direction as a function of its angle of incidence (Fig. 2.2).

Remarkably, directionality is substantial, with inter-antennal velocity differences that were up to 25 dB at 140 Hz [see explanations of the estimation of the intensity of inter-antennal differences in Morley et al. (2012)]. For an organism whose auditory receivers are separated by only  $660 \pm 51 \mu\text{m}$  (mean  $\pm$  S.D.), this inter-antennal velocity difference is far greater than differences in intensity observed between tympanal ears for organisms of similar sizes.

Combining these measurements with a laser vibrometry analysis of the vibratory movement of the arista, Morley et al. (2012) demonstrated that the mechanical sensitivity of the antennae changes as a function of the angle of incidence of the acoustic stimulus, with peak responses along axes at 45 and 315° relative to the longitudinal body axis.

This work indicates not only that flies are able to detect a difference in signal intensity according to its direction, but also that the male song structure may not be the sole determinant of mating success; the male spatial position also makes a major contribution to female sound reception and therefore also, perhaps, to her decision making.

## 2.3 Macro-PIV at the Receptors Scale ( $10^{-4}$ m Resolution)

Rigorous understanding of the performance of a sensor generally requires studying the interaction between the input signal and the sensory organs. Airflow sensing by filiform hairs partially immersed in the boundary layer around the body has been extensively studied in arthropods, and especially spiders and crickets (Shimozawa and Kanou 1984; Humphrey et al. 1993; Barth et al. 1993; Bathellier et al. 2012). Filiform hairs can respond to air velocities as small as  $0.03 \text{ mm s}^{-1}$  (Shimozawa and Kanou 1984), making them one of the most sensitive biological sensors in the animal kingdom (Shimozawa et al. 2003). These outstandingly sensitive structures are used to detect the faintest oscillatory signals produced by the wing beats of prey and predators (Tautz and Markl 1979; Gnatzy and Heusslein 1986; Magal et al. 2006; Steinmann et al. 2006; Casas et al. 2008). The presence of hairs of different lengths allows spiders and crickets to fractionate both the intensity and frequency range of an airflow signal.

Several flow measurement techniques have been exploited to investigate the flow around a sensory hair, or sensory hair deflection, in terms of both phase and

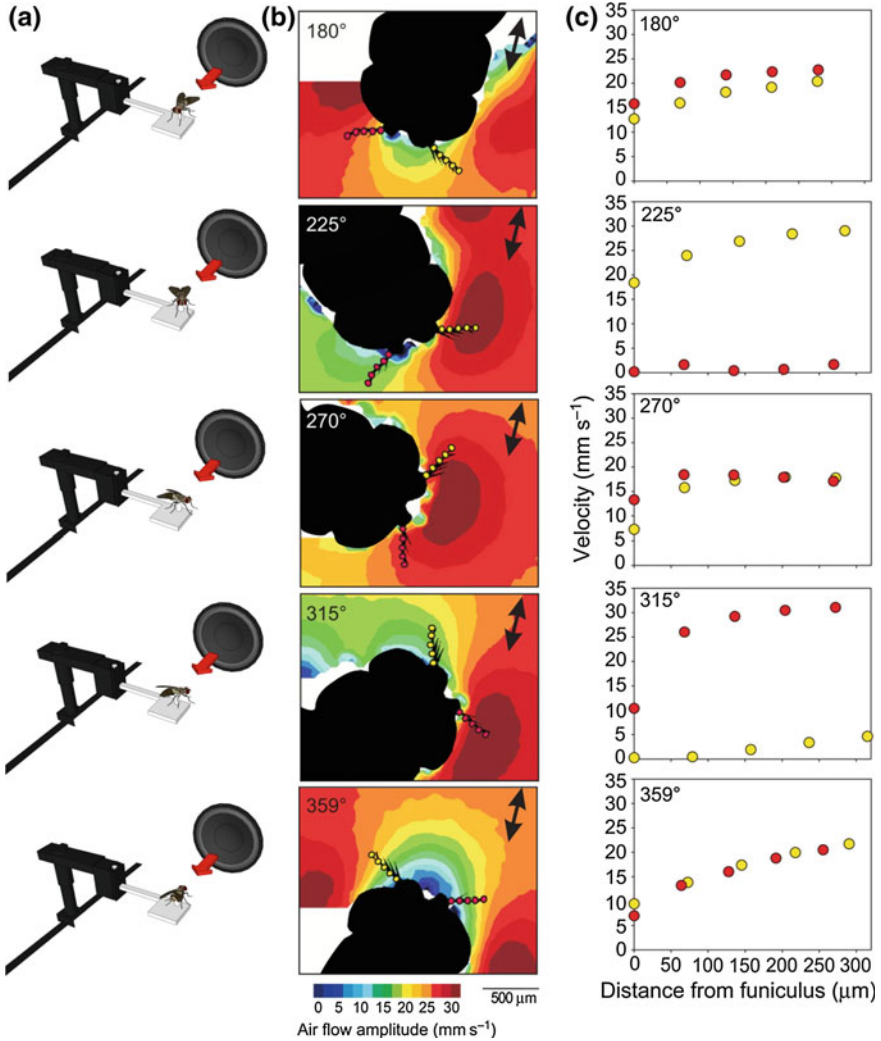


**Fig. 2.2** **a** Orientation of *Drosophila melanogaster* to a 140 Hz sinusoidal stimulus produced by a loud speaker. **b** PIV velocity maps for five stimulus angles around the head of one individual fly. Points along the aristae correspond to positions at which velocity was determined. Large black arrows indicate the direction of the stimulus source. **c** Extracted velocity at five points along each arista for angles corresponding to those in (a). Yellow points represent the left arista, red points represent the right arista

frequency. In a pioneering study, Barth et al. (1993) adapted LDA to the study of the boundary layer of the flow over a spider leg. Kämper and Kleindienst (1990) and Shimozawa et al. (1998) adapted laser vibrometry to allow measurement of the deflection of cricket hairs.



In water, diverse animals use arrays of hair-like structures for important tasks such as feeding, gas exchange, smelling, and swimming. Koehl used both dynamically scaled physical models and a custom made PIV to study the flow through hairy food-capturing appendages (second maxillae) of calanoid copepods, which are abundant planktonic crustaceans (Koehl 2004). More recently, small-scale PIV has been used to show that antennule morphology and flicking kinematics facilitate odor sampling by the spiny lobster (Reidenbach et al. 2008). PIV has also been used to determine the fine-scale patterns of odor encounter by the antennules of mantis shrimps tracking odor plumes in both wave-affected and unidirectional flow conditions (Mead 2003). Mc Henry et al. (2008) presented direct PIV measurements of mechanical filtering by the boundary layer and fluid-structure interaction in the superficial neuromast of the fish lateral line system.

Following adaptation of PIV to small scales in water, we describe below how we adapted standard PIV protocols for the study of flow in air at a similar small scale. The major differences between macro-PIV and classical PIV are the use of a specialized optical system producing a particularly thin sheet of laser light and of a lens with five-times magnification.

### 2.3.1 Experimental Instrumentation

Various types of sample, including the cercus of *Nemobius sylvestris*, single 1,000  $\mu\text{m}$ -long micro-electromechanical system (MEMS) hairs, and tandem 1,000  $\mu\text{m}$ -long MEMS hairs on a plate of dimension  $10 \times 10 \text{ mm}^2$  (Krijnen et al. 2006) were placed in a glass container (dimensions:  $10 \times 10 \times 10 \text{ cm}^3$ ), with one loudspeaker (40 W) on one side connected to a signal generator. The seeding of air, the laser sheet generation and the imaging is explained in Sect. 2.2.1. The target area was then imaged onto the CCD array of a digital camera ( $696 \times 512$  pixels) using a binocular lens that allowed observation of a  $2 \times 2 \text{ mm}^2$  window around the substrate. The measurement technique is illustrated in Fig. 2.3. Far-field velocities were in the range 10–50 cm/s and flow frequencies 40–320 Hz. We used a stroboscopic principle to sample high frequency oscillatory flow signals with a PIV system limited to 20 Hz (Steinmann et al. 2006).

This technique allowed us to analyze the flow at a relatively high spatial resolution, higher than possible with standard PIV methods. We obtained a whole measurement field of  $2,000 \times 2,000 \mu\text{m}$  with a 5X magnification binocular objective lens. Given the camera resolution ( $696 \times 512$  pixels), the resolution can be  $2.87 \mu\text{m}/\text{pixels}$ . Thus, selecting a 32-pixel correlation area, the spatial resolution is  $100 \mu\text{m}$ . Using a time interval of  $500 \mu\text{s}$  between two images and a sub-pixel interpolation, we were able to follow particle displacements of  $0.287\text{--}100 \mu\text{m}$ . This methodology can thus resolve flows between 0.3 and 30 mm/s. The depth of field is given by the thickness of the laser light sheet and is estimated to be almost  $\Delta z = 50 \mu\text{m}$  at the focus point.



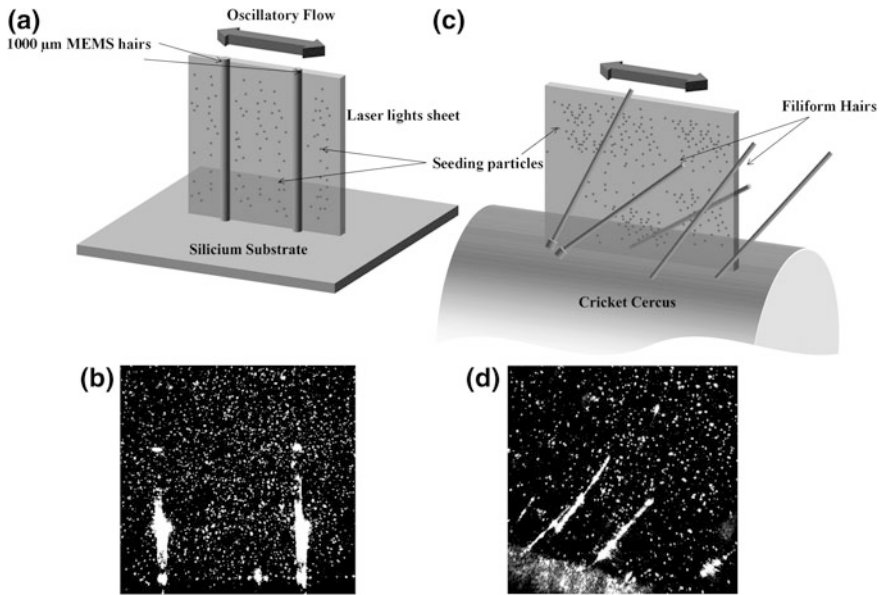


**Fig. 2.3** Illustration of the macro-PIV principles. **a** PIV with a silicium substrate covered with MEMS hairs. **b** Raw PIV image of the seeding particles in the plane formed by the two MEMS hairs. **c** The same PIV technique adapted for the measurement of the oscillatory flow over a cricket cercus within the filiform-hair canopy. Filiform hairs are not always in the measurement plane, and sometimes cross it. **d** PIV images of the seeding particles in the light sheet plane. Hairs are in fact longer than can be observed on the image, but parts of their lengths are outside the light sheet

The quality of the measurement is greatly affected by the tracer concentration: if the concentration is too high, the discrimination of individual particles will be nearly impossible; if the concentration is too low, the particle density will not be sufficient for accurate estimation of the velocity at each point in the whole cross section of the flow. Indeed, the concentration must be lower than (Adrian and Westerweel 2011):

$$C_{\max} = \left(\frac{M}{d_i}\right)^2 \frac{1}{\Delta z}$$

where  $M$  is the magnification,  $d_i$  the particle diameter and  $\Delta z$  the laser light sheet thickness. As we will see in the next chapter on micro-PIV, there is a relationship between the signal-to-noise ratio (SNR) and the thickness of illumination (here referred to as the ‘laser light sheet thickness’, and also called ‘the test section depth’).

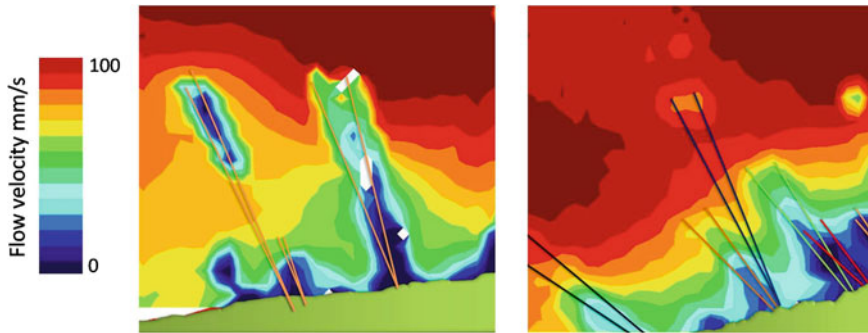


**Fig. 2.4** Amplitude of an oscillatory flow over a canopy of cricket filiform hairs (Frequency = 80 Hz, Amplitude = 100 mm/s). Measurements from two different locations on the cercus are shown

### 2.3.2 Application of (Conventional) Macro-PIV to Airflow Sensing Organs

#### 2.3.2.1 Cricket Hair Canopy

Figure 2.4 shows the velocity amplitudes of the oscillatory flow over a cricket cercus at two different locations. These findings reveal the complex arrangement of cricket filiform hairs and the corresponding flow patterns that result from the interactions between the boundary layers of different filiform hairs.

The mechanical constraints of the socket at the base of cricket filiform hairs cause a preferential plane of deflection, i.e. directionality. For a given direction of an incoming flow, only some hairs will oscillate in this flow direction, rather than in the plane of the laser sheet. Since it is impossible to determine the exact geometry and the plane of motion of the dense hair canopy in the immediate vicinity of the measurement plane, the interpretation of the flow patterns revealed by the PIV measurement is limited. The “out of plane” hairs probably have a large influence on the flow in the section of measurement. Nevertheless, it is still possible to extract some information about the ability of the hairs to follow the flow. The use of a stroboscopic technique to sample high frequency oscillatory flow allows simultaneous assessment of the dynamics of the flow velocity surrounding the cercus and the angle of displacement of the hairs (see Fig. 2.5).

Hairs of different sizes will be differently out of phase with the far-field flow. In the experiment illustrated, the small hair seems to have a phase advance of  $26^\circ$  with respect to the far-field flow. At a stimulus frequency of 80 Hz, as used here, a phase advance agrees well with the velocity of air within the boundary layer, in which the  $260\text{ }\mu\text{m}$ -long hair is totally immersed, being phase advanced by  $\pi/4$  (Kumagai et al. 1998; Steinmann et al. 2006). By contrast, the longer hairs ( $430$  and  $1,070\text{ }\mu\text{m}$ ) were not totally immersed in this boundary layer and were

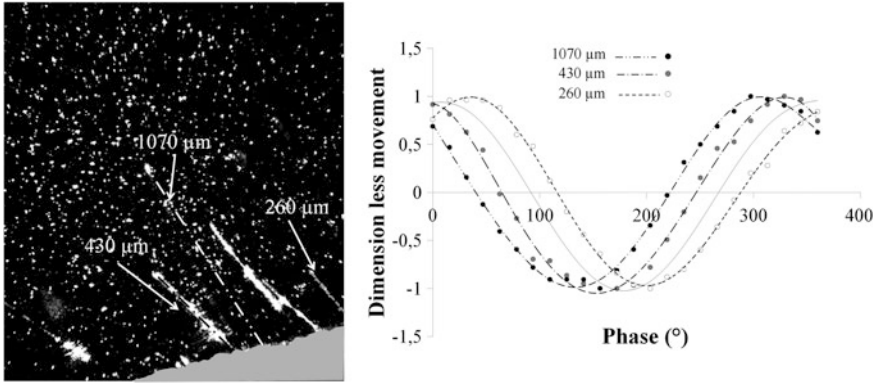


**Fig. 2.5** (Left) Position and size of 3 filiform hairs, of length of 430, 1,070, 260  $\mu\text{m}$ . (Right) Comparison of the phase differences between the far-field flow (gray line) and the three hairs. The gray line represents the phase of the far-field flow measured 1,500  $\mu\text{m}$  above the cercus surface. The movements of the hairs are dimensionless, their velocity being divided by their maximal velocity. The hair length refers to the visible length and is therefore subject to error

thus less subject to this phase advance: indeed, they showed a phase lag ( $-26^\circ$  for the 430  $\mu\text{m}$ -long hair and  $-51^\circ$  for the 1,070  $\mu\text{m}$ -long hair). At 80 Hz, such increases of the phase lag with the length of the hair are expected and are coherent with theory. Although they are interesting in themselves, these results cannot be easily generalized. Systematic experimental variation of parameters is not feasible, as it is nearly impossible to find appropriate spatial arrangements of hairs in rows and similarly unlikely that each hair of such rows moves within the plane.

### 2.3.2.2 Single Cricket Hairs

We applied the macro-PIV technique in combination with a novel compact theoretical framework to describe the cricket hair mechanics (Fig. 2.6). In a systematic fashion, we studied the ability of six hairs of different lengths (410–870  $\mu\text{m}$ ) to follow oscillatory flows between 30 and 300 Hz (Bathellier et al. 2012). We found that cricket air-motion sensing hairs (and those in spiders) work close to the physical limit of sensitivity and energy transmission across a broad range of relatively high frequencies. In this range of frequencies, the hairs closely follow the motion of the incoming flow because a minimum of energy is dissipated in their basal articulation. This frequency band depends on hair length, and is between about 40 and 600 Hz, which is beyond the frequency at which the angular displacement of the hair is maximal.

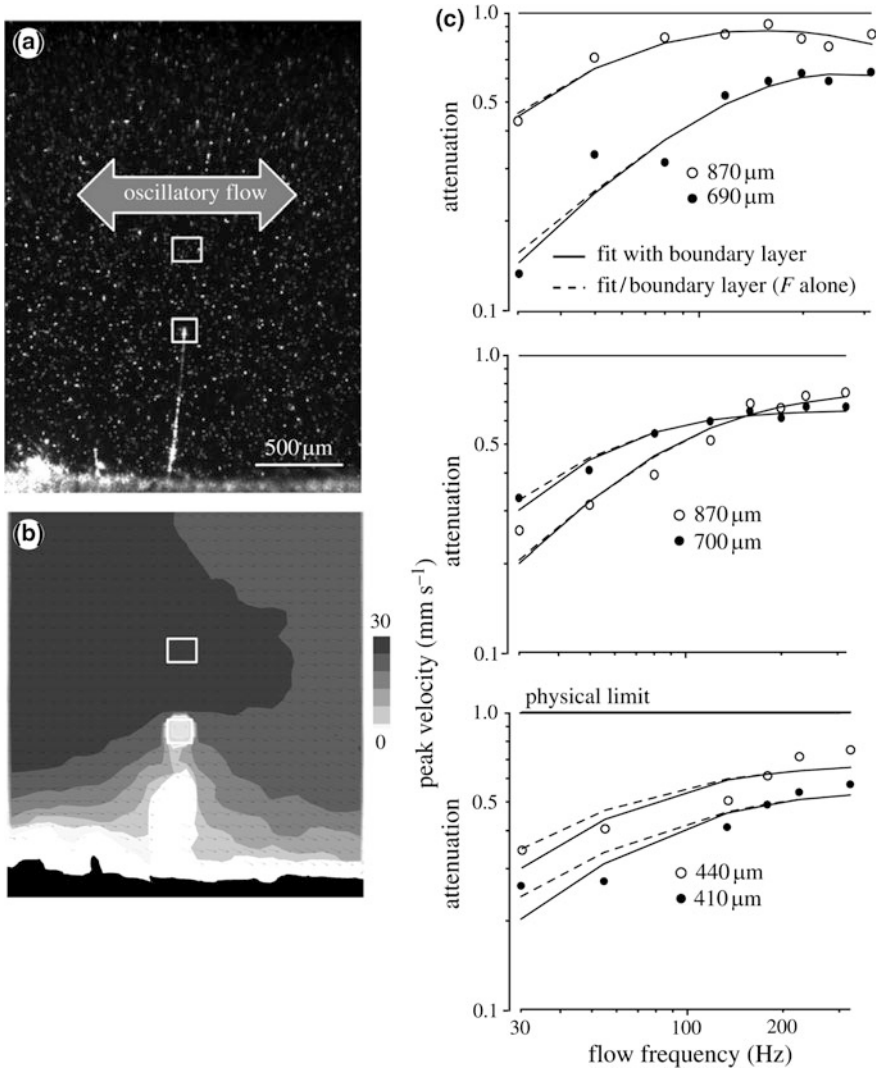
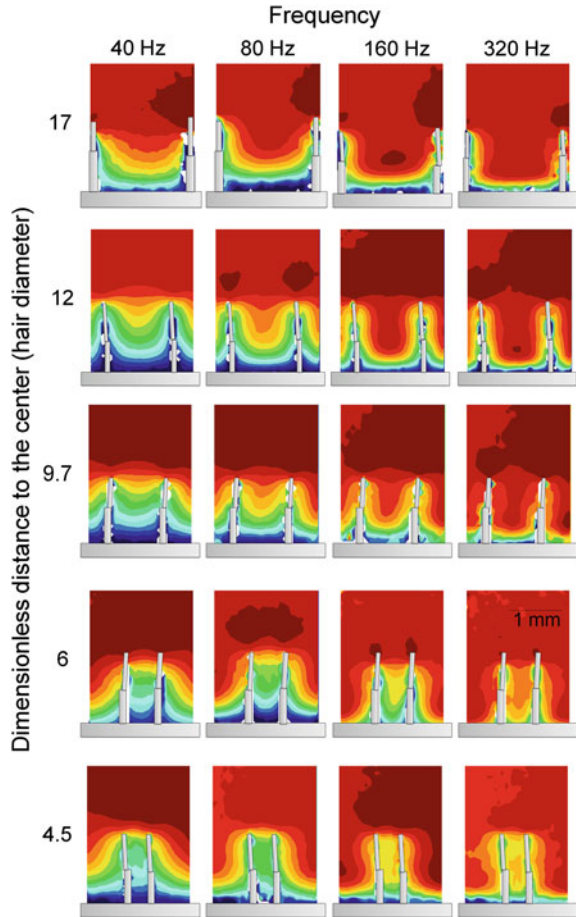


**Fig. 2.6** Measurements of filiform hair motion in the cricket *Nemobius sylvestris*. **a** Picture of a cricket cercal hair in macro-PIV recording chamber. **b** Map of instantaneous air particle velocity (grey scale) and direction (arrows) for a 80 Hz oscillatory flow. The white squares represent the areas selected to compute the far-field flow velocity and the hair-tip velocity, respectively. **c** Deviation from the physical limit calculated by dividing the tip velocity of the hair measured by PIV by its physical limit, for six isolated cricket cercal hairs of different lengths. The solid lines represent the fit of the transfer function of a 2nd order mechanical system. In this model, the effect of the boundary layer was taken into account. It simply translates into a reduction of velocity close to the cercus surface (Bathellier et al. 2012)

**Fig. 2.7** Full-field data for flow in the vicinity of 1 mm-long MEMS hairs arranged in tandem, as a function of the frequency and inter-hair distance. Color code as in Fig. 2.6



### 2.3.2.3 The Use of MEMS Hairs as a Surrogate

Investigations of the flow around natural filiform hairs suffer various limitations: it is difficult to select hairs of the desired lengths and to find tandem hairs with parallel planes of vibration. By using MEMS artificial sensors mimicking biological counterparts, it is however possible to reduce the various uncertainty factors. Indeed, all the MEMS hairs have a same, fixed length, and the use of MEMS technology enables very simple geometrical arrangements to be obtained, such as isolated hairs or tandem hairs with different spacing between the two members of the pair. By using flat plate substrates, all the nonsolvable problems arising from the 3D geometry of the cercus that supports the hairs in vivo can be avoided or minimized.

We used the PIV technique to measure the extent of flow perturbation by single and tandem hairs directly, using MEMS hairs as physical models (Fig. 2.7). Single

and tandem MEMS hairs with various inter-hair distances were subjected to oscillatory flows of diverse frequencies. Decreasing hair-to-hair distance markedly reduced flow velocity amplitude and increased the phase shift between the far-field flow and the flow between hairs. These effects were stronger for lower flow frequencies. We therefore predict strong hydrodynamic coupling within natural hair canopies exposed to natural stimuli, and the effects will vary depending on species, hair sizes, and hair densities (Casas et al. 2010).

### 2.3.3 Limitations of the Macro-PIV Technique

Kähler et al. (2012) reviewed the major sources of uncertainty of PIV near surfaces. They identified four major factors that determine the ability to resolve the flow in the hundreds of micrometers closest to the boundary layer: (1) the use of appropriate tracer particles that follow the fluid motion with sufficient accuracy, (2) the use of fluorescent particles or tangential illumination, such that reflection from the wall can be eliminated or avoided, (3) appropriate imaging of the particles with a lens or a microscope objective such that the particle signal can be suitably captured on a digital camera, and (4) satisfactory estimation of particle image displacement with digital particle imaging analysis methods. In our experiments, we had to deal with two of these four uncertainty factors, the imaging of individual particles and wall reflection. Indeed, one of the most important factors limiting the spatial resolution of the technique is diffraction: the recorded image of a tracer particle is generally greater than its theoretical magnified size (Meinhart et al. 2000). The size of the particle image is mostly determined by the diffraction of the optical system. Let  $d_i$  be the particle image diameter given by:

$$d_i = \sqrt{M^2 d_p^2 + d_{\text{Diff}}^2}$$

where  $M$  is the linear magnification of the binocular lens,  $d_p$  is the particle diameter (200 nm for DEHS oil droplets) and

$$d_{\text{Diff}} = 2.44(1 + M)\lambda \frac{1}{2\text{NA}}$$

where  $\lambda$  is the laser wavelength (532 nm) and NA is the numerical aperture of the optical system (binocular lens) and is 0.1 in our case.

It is also important to note that  $d_i$  is the size of the particle as projected onto the camera CCD sensors. Thus, the size of this particle in the measurement field will also depend on the size of the CCD sensor (see Fig. 2.8). As an example, with a 5X magnification, the field of view is 2,000  $\mu\text{m}$  and consequently each pixel corresponds to  $2,000/696 = 2.87 \mu\text{m}$ . At the measurement field scale, the particle image size is  $3.24 \text{ pixels} \times 2.87 \mu\text{m/pixels} = 10 \mu\text{m}$  (Fig. 2.8).

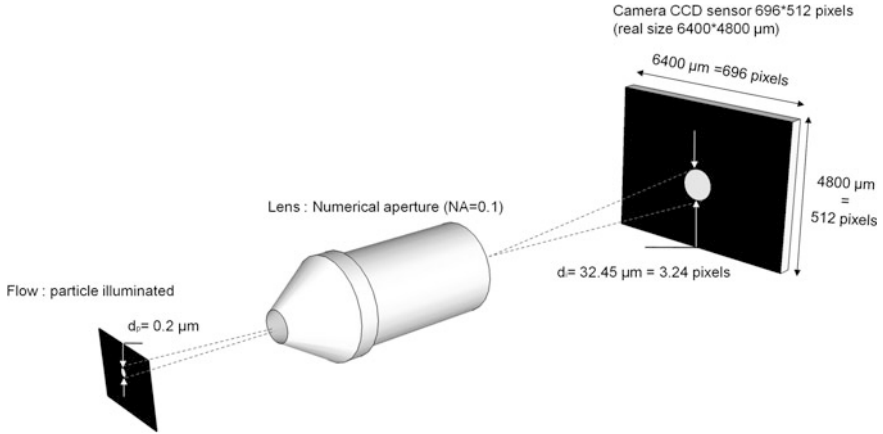


**Fig. 2.8** Explanation of the estimation of the particle image size

Another limitation results from the large amount of light re-emitted by the surface of objects present in the flow. Biological sensory organs are generally very small, and therefore the capacity of the technique to resolve flows within a few hundred microns of the surface is crucial.

## 2.4 Micro-PIV at the Scale of Biological Receptors ( $10^{-5}$ m Resolution)

We have shown that the macro-PIV technique has limitations, in terms of spatial resolution, due to the small magnification factors of the optical system used. But even if magnification were to be increased, macro-PIV would still be limited by both the large diffraction of the optics and the substantial reflection from the surfaces of the objects studied. These constraints prevent visualization and quantification of the flows very close to receptors.

We will show in this section that using volume illumination provided by an epifluorescent microscope instead of the conventional optical light sheet allows the analysis of microscopic flows at the required scale (Santiago et al. 1998). In this methodology, the light, provided by a double pulsed monochromatic Nd:YAG laser (532 nm) is reflected by a dichroic mirror, travels through an objective lens that focuses on the point of interest, and illuminates a volume seeded with fluorescent particles. The emission from these particles at a specific wavelength (560 nm), along with the reflected laser light coming from surfaces or interfaces, shines back through the objective, the dichroic mirror and through a band pass filter that blocks the specific wavelength of the laser light (Wereley and Meinhardt 2010).

The ability to observe and analyze a plane in macro-PIV is a consequence of the planar nature of the laser sheet that illuminates only a cross section of the flow.



By contrast, micro-PIV is a volume illumination technique, and exploits the ability of the objective lens to focus on a single plane, such that there is a two-dimensional plane in which particles can be viewed. Nevertheless, with this illumination method, the entire depth of the section is illuminated by a cone of light. Consequently, there is often background noise due to the emission from the out-of-focus particles added to the emission of individual particles in the focus plane; this can make discrimination difficult and low seeding concentrations have to be used. In the next section, we describe averaging analysis techniques that must be employed with this technique due to the low seeding. One consequence is that only steady flows can be investigated, in contrast to more conventional PIV techniques which can be used with unsteady or oscillatory flows. Adapted preprocessing techniques must also be used because the images tend to have a zero-displacement bias from background noise and low signal-to-noise ratios. Also, because of the low seeding particle density, high numerical aperture objectives are required to capture as much of the light emission as possible. The choice of optical material is therefore critical.

As far as we know, micro-PIV has rarely, if ever, been applied in the field of sensory ecology. The following section illustrates our attempts to apply this new technique to the visualization and quantification of the flows around single natural and biomimetic hairs with a resolution of 10  $\mu\text{m}$ .

### ***2.4.1 Experimental Instrumentation***

The experimental micro-PIV apparatus consisted of a liquid delivery system composed of a syringe pump, a laser system, an epifluorescent microscope, an objective lens and an imaging system, and the cercus sample placed in a test section (a cavity with dimensions: 10 mm  $\times$  5 mm  $\times$  500  $\mu\text{m}$  in PVC plate). Illumination was provided by a twin Nd:YAG laser system. The laser beams were directed onto the cercus using an objective lens (Olympus X20 or X40). The laser produces pulses of green light (532 nm) re-emitted by the fluorescent tracer particles at 560 nm. The tracer particle images were captured with a PCO Sensicam camera (696  $\times$  512 pixels) and the images were transferred to a computer for processing. The camera and the laser were synchronized via an ILA PIV Synchronizer. The cercus was placed in a small waterproof Plexiglass box (500  $\mu\text{m}$  depth) seeded with fluorescent particles (RhB-labeled beads of  $d_p = 360$  nm). The box was open on both sides to allow a continuous flow.

#### **2.4.1.1 Resolution of the Technique**

This technique allowed us to acquire high-resolution tracer particle images. We obtained, with a 20X objective lens, a measurement field of 440  $\times$  330  $\mu\text{m}$ . With a 40X objective lens, the measurement field was 220  $\times$  165  $\mu\text{m}$ . The time

between two laser impulses was set at 500  $\mu\text{s}$ , to resolve relatively high speed flows. Using the method described in [Sect. 2.3.1](#), we determined that, for a 20X magnification, spatial resolution was 10  $\mu\text{m}$  and flows between 0.13 and 13 mm/s could be studied.

### 2.4.1.2 Depth of Field and Measurement Depth

For 10  $\mu\text{m}$  resolution in the focus plane, the depth of field and the measurement depth have to be limited to the same scale. However, the generation and alignment of a light sheet thinner than 50  $\mu\text{m}$  is not possible, and therefore the use of volume illumination is the only feasible approach (Meinhart et al. 2000). In macro-PIV techniques, the depth of field is determined by the thickness of the laser light sheet, and the measurement depth by the positioning of the light sheet. By contrast, for volume illumination techniques, the depth of field and the measurement depth must be carefully determined.

The depth of field, which is the distance between the nearest and farthest objects that appear acceptably sharp can be calculated by Inoue and Spring (1997):

$$\delta_z = \frac{n\lambda}{\text{NA}^2} + \frac{ne}{\text{NAM}}$$

where  $n$  is the refractive index of the fluid between the objective lens and the test structure,  $\lambda$  is the wavelength of the incident light, NA is the numerical aperture of the objective lens,  $M$  is the total magnification of the microscope system, and  $e$  is the smallest resolvable distance on the image detector, i.e. the spacing between pixels. In the experimental setup we used,  $n = 1$  for air,  $\lambda = 532$  nm,  $\text{NA} = 0.40$ ,  $M = 20$ , and  $e = 0.64$   $\mu\text{m}$ , resulting in a depth of field of  $\delta_z = 3.4$   $\mu\text{m}$ .

The measurement depth is the distance from the center of the object plane beyond which the particle image intensity is too low to contribute significantly to the measurement. It is given by Meinhart et al. (2000):

$$\delta_{z_m} = \frac{3n\lambda}{\text{NA}^2} + \frac{2.16d_p}{\tan \theta} + d_p$$

where  $d_p$  is the tracer particle diameter (for RhB-labeled beads,  $d_p = 360$  nm) and  $\tan \theta = \text{NA}/n$ . With the optical settings we used,  $\delta_{z_m} = 12.3$   $\mu\text{m}$ .

For our experimental setup, the measurement depth was larger than the expected depth of field. We therefore had to keep the depth estimation criteria that gave the largest numerical result.

### 2.4.1.3 Air and Water Similitude

Micro-PIV has typically and historically been used in water, whereas cerci and hairs are naturally in air. At constant temperature (27 °C), the kinematic viscosity

of air is 20 times greater than that of water. The Stokes boundary layer thickness depends on this kinematic viscosity as follows:

$$\delta_{BL} = \frac{4.64D}{Re^2}$$

where  $D$  is the diameter of the object being considered, i.e. the cercus or the hair diameter, and  $Re$  is the Reynold's Number defined thus:

$$Re = \frac{UD}{\nu}$$

where  $U$  is the velocity of the fluid and  $\nu$  is the kinematic viscosity of the fluid.

There is a simple relationship between the kinematic viscosity of air,  $\nu_{air}$ , and the kinematic viscosity of water,  $\nu_{water}$ :

$$\nu_{air} = 20 \nu_{water} \text{ at } 27^\circ\text{C}$$

Consequently, at the same fluid velocity, the boundary layer thickness is 4.5 times smaller in water than in air. During our study, we therefore produced a continuous water flow of 2 mm/s which is equivalent to a 40 mm/s flow in air. The value of 40 mm/s is a biologically relevant value for crickets: it is the flow produced in front of a running spider (Casas et al. 2008).

## 2.4.2 Application of the Micro-PIV Technique to Airflow Sensors in Crickets

### 2.4.2.1 Study of Cercus Roughness and the Influence of Setae

The cricket cercus is covered with setae and small spines, up to a few tens of microns long, implanted at high density. The denticles covering shark skin reduce drag by decreasing the vorticity and shear stress in the boundary layer (Bechert and Bartenwerfer 1989; Bechert et al. 2000; Lee and Lee 2001). The drag reduction is proportional to the denticles size, but for larger denticles the proportionality breaks down, and the drag reduction eventually becomes a drag increase (Garcia Mayoral and Jimenez 2011). By analogy, we expected the spines on the cricket cercus to modify the boundary layer in the first hundreds of micron surrounding the cercus (Fig. 2.9).

Indeed, the modification of the boundary layer caused by the setae tends to extend to 150  $\mu\text{m}$  above the cercus surface (Fig. 2.9b), a distance three times longer than the average length of the setae and long enough to be relevant to many sensory hairs. For a meaningful interpretation, these measurements of the biological system should be compared to the corresponding measures for a smooth cylinder surface. The experimental boundary conditions are, however, very difficult to estimate because they involve a superposition of the boundary layers of the

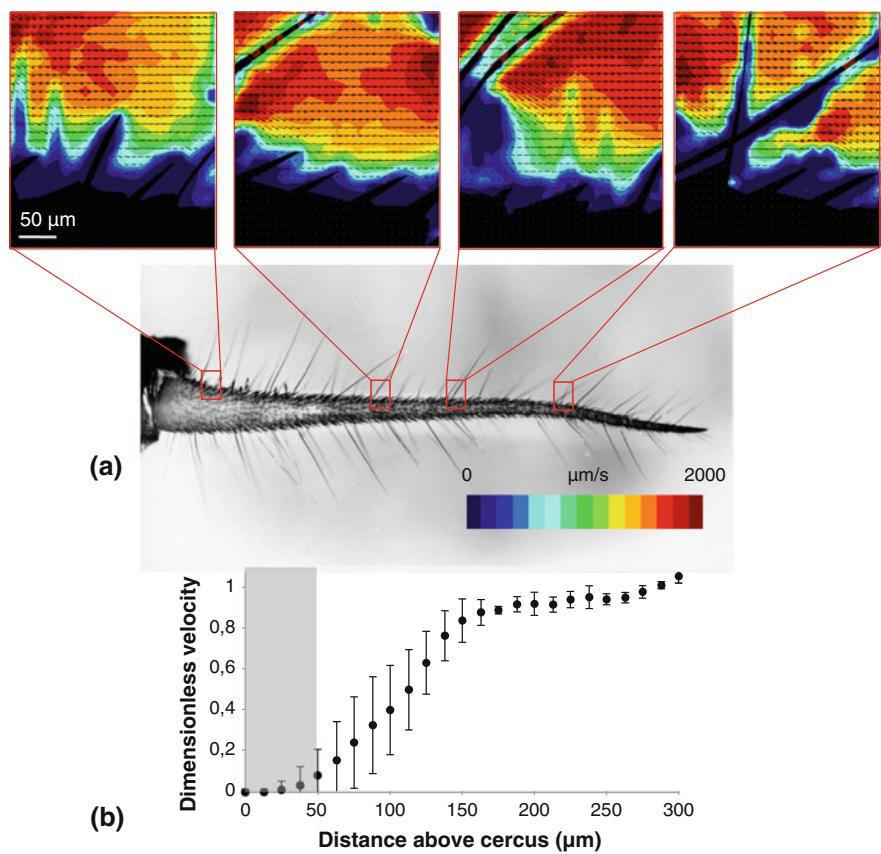


**Fig. 2.9** Velocity fields of the flow in the first 500  $\mu\text{m}$  around a cricket cercus acquired with the micro-PIV setup at four positions along a cricket cercus immersed in a water (a). Profile of the average flow over a vertical profile at the 4 positions. The distance is estimated from the base of the setae, and the average length of the setae is represented by the grey box (b). Velocities are normalized to the far-field velocity

channel test chamber with that of the cercus. Finally, the micro-PIV technique can only be used in water and water promotes adhesion of the seeding particles to the cercus surface and to each other (agglomeration).

#### 2.4.2.2 Visualization and Quantification of the Flow Over a Single Hair

The micro-PIV technique was used to visualize and quantify the flow velocity over a single hair in steady flow at three different velocities: 150, 1,000, and 3,000  $\mu\text{m/s}$ . Figure 2.10 shows the velocity field of a continuous flow along a cercus. The hair in the measurement plane had a 10  $\mu\text{m}$  diameter. Two boundary layers can be seen, one around the cercus and the other around the hair. The flow was disturbed around

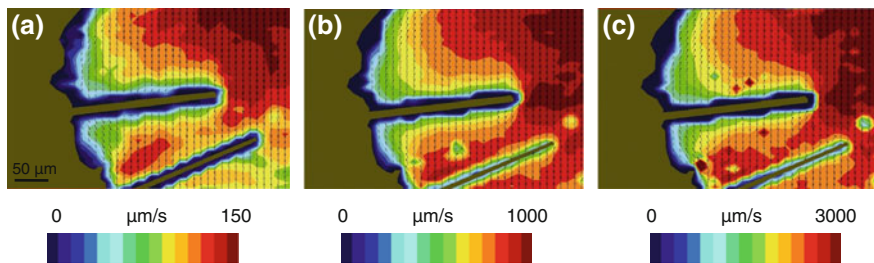


**Fig. 2.10** Velocity field around a 10  $\mu\text{m}$ -diameter cricket filiform hair (in the *middle* of each picture) in steady flows at three different velocities corresponding to three different regimes:  $V = 150 \mu\text{m/s}$ ,  $Re = 0.002$  (a),  $V = 1,000 \mu\text{m/s}$ ,  $Re = 0.015$  (b),  $V = 3,000 \mu\text{m/s}$ ,  $Re = 0.045$  (c)

the hair to a distance of roughly 15 times its diameter. Such strong disturbances over a long distance are comparable to what we observed previously for larger MEMS hairs, suggesting strong hydrodynamic coupling within natural hair canopies, depending on arthropod hair sizes and density (Casas et al. 2010).

#### 2.4.2.3 Steady Flow Over a MEMS Hair

We adapted the micro-PIV technique for investigation of the steady flow along a single MEMS hair (Fig. 2.11). A set of 50 image pairs of the seeding particle flow in a cross section around a hair was obtained. After processing the micro-PIV images for reduction of noise, we used image pairs to compute the correlations to determine the local velocities of the particles. Figure 2.11d is the result of the averaging of the 50 velocity fields.

### 2.4.3 The Challenges for the Use of Micro-PIV in Sensory Ecology

It is clear that there are numerous problems associated with the adaptation of the micro-PIV technique to applications in sensory ecology, as illustrated above. The use of fluorescent particles and the background noise due to the volume illumination both limit the application of this technique to 2D flow in very simple setups. In most cases, the images are very noisy, such that it was not possible to identify individual particles. The reasons for this large amount of noise are numerous. We present here the three principal problems we had to face and suggest ways to solve them.

#### 2.4.3.1 The Depth of the Micro Channel

Mielnik (2003) provides an estimated relationship between the SNR as function of the particle concentration and the depth of the test section. An increase of the

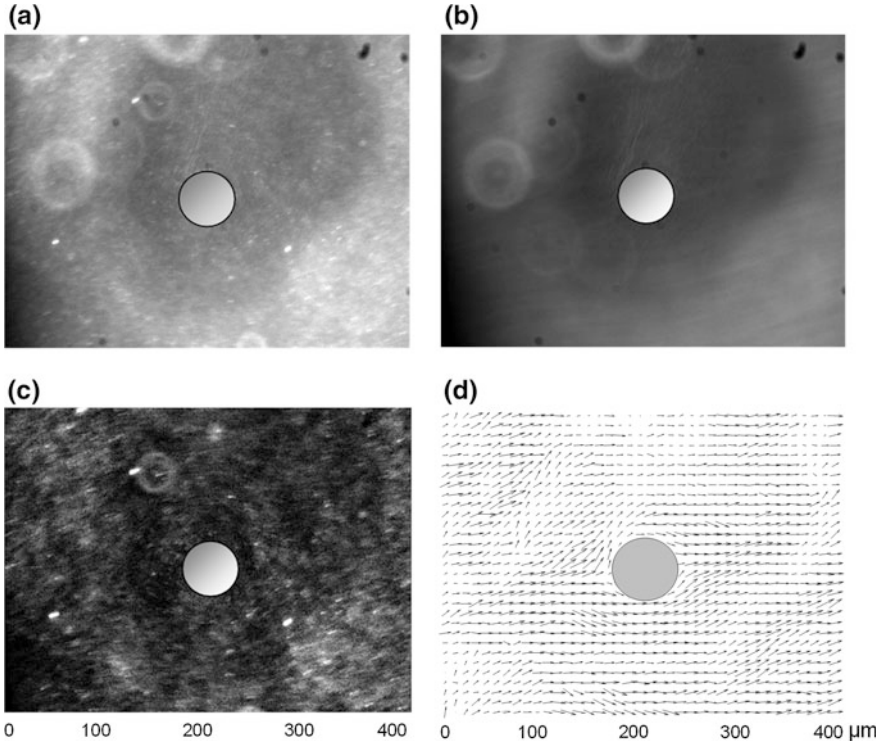


**Fig. 2.11** Raw micro-PIV image of the particles around a MEMS hair (a), constant background extracted by estimating the minimal *gray* value by a technique of pixel-by-pixel sliding over time (b), pre-processed image (c) and velocity field around a hair in a viscous steady flow from the *left* (d)

micro channel depth or an increase of the particle concentration leads to a decrease of the SNR. The author estimated that test section depths larger than 200  $\mu\text{m}$  would not allow a sufficient SNR, even at very low particle concentration (lower than 0.01 %). We concluded that the cercus was too thick (between 300 and 500  $\mu\text{m}$ , which is thicker than most micro-channels) to provide good measurements because the SNR is very low. A solution to this problem could be to place a small cross section of the cercus in a very shallow micro-fabricated channel.

#### 2.4.3.2 Particle Density

As explained by Mielnik (2003), a reduction of the particle density also leads to an increase of the SNR. Beyond a certain density, seeding particles are too few to provide enough information about the flow velocity at a sufficiently high spatial resolution. Micro-PIV experiment designs have to address this trade-off, lowering the particle density while generating sufficient information. The constraint imposed by the large section depth in our setup made it impossible to find a

suitable concentration. Mielnik et al. (2006) developed a novel seeding method, called Selective Seeding. The method involves selective seeding of a thin fluid layer within an otherwise particle-free flow. By analogy to the laser sheet in macro scale PIV, such particle sheets define both the depth and the position of the measurement plane, independent of the details of the optical setup.

It is also possible to make measurements in deep micro channels by confocal micro-PIV (Lima et al. 2007). This technique is based on confocal microscopy, in which pinhole apertures are used for spatial filtering and thus optical sectioning. As a result, it is possible to obtain a series of optical sectioning images at different focal planes, which provides 3D information of the fluid flow and reduces considerably the amount of background noise.

### 2.4.3.3 Contrast and Particle Fluorescence

The fact that individual particles are often not visible could also be due to insufficient fluorescence of the particles, or to poor transmission through the optical system of a given wavelength. We carried out experiments with three kinds of particles from micro-particles GmbH: PS-Rhodamine B-particles (Diameter = 439 nm), MF-Rhodamine B-particles (Diameter = 366 nm), and PS-RhB-PEG-particles (Diameter = 448 nm). All these different particles absorb light at 560 nm and re-emit it at 584 nm. The results were similar for the three kinds of particles. We also tried different objective lenses, without improving the results.

### 2.4.3.4 Particles Agglomeration

We were able to increase the SNR by using a nonionic surfactant, polyvinyl alcohol, and alternatively by using seeding particles with a surface treatment (Polystyrene Rhodamine B particles, treated with Poly Ethylene Glycol). These two solutions greatly reduce both particle agglomeration and the sticking of particles to the walls of channels.

The noise has also been reduced computationally by subtracting a sliding minimum over time, for each pixel independently. The background noise stays the same over all images, while seeding particles move. This operation is executed with a window length of 30 images. For a particular pixel at a given position in image ( $n$ ), the minimum over all images at that position is calculated and then subtracted from the pixel intensity in image ( $n$ ) to obtain an enhanced processed image.

## 2.5 Conclusions: The Way Forward

This survey addresses micro-PIV in particular, as this technique had not previously been used in the field of sensory ecology. Being both novel and having unmatched accuracy, micro-PIV inevitably has great potential. However, our application of



this approach to the analysis of cricket sensory hairs has revealed several problems inherent to the technique. Solutions could often, but not always, be found.

Are these or similar problems encountered in other fields of application and how are they solved there? We performed a survey of the many papers published with micro-PIV technology to answer these questions (Appendix Table 2.1). As Wereley and Meinhart (2010) recently estimated, over 100 papers have been published annually reporting the use of this technique. Our survey shows that the problems we encountered are by no means rare. It also reveals that most of these studies were conducted in very small micro channels of thicknesses smaller than 500  $\mu\text{m}$ , usually between 10 and 200  $\mu\text{m}$ . Thus, one has to conclude that micro-PIV is a technique suitable for simple, essentially two-dimensional problems. This can be understood historically, as micro-PIV development was motivated by the need for a methodology to investigate microfluidic viscous flow phenomena. The broader utility of micro-PIV was demonstrated subsequently by applying it to flows in microchannels, micronozzles, BioMEMS, and flows around cells, still essentially 2D structures. Most sensory ecological issues associated with higher organisms are three-dimensional, and consequently micro-PIV is intrinsically not well adapted.

Combining the advantages of classical PIV and micro-PIV (see Appendix Table 2.2 for a comparison) would in many ways be a suitable solution for most of the problems and enable sensory ecologists to work at the receptor scale. There are indeed ways to adapt micro-PIV technology to suit the needs of sensory ecology. One very recent advance is to use confocal techniques (see Lima et al. 2007 and Patrick et al. 2010). However, this development is currently too expensive and sophisticated for most sensory ecology laboratories. Another possibility for channel depths larger than 1 mm is based on traditional laser light sheet illumination combined with long distance microscopic, rather than volume illumination. For an overview of this method see Kähler et al. (2006) and the most recent work by Alharbi and Sick (2010) and Eichler and Sattelmayer (2011). These authors explain that using a telecentric lens instead of a typical microscope solves the problem of the background noise caused by unfocused particles. The depth of focus of the optical system is then larger than the thickness of the laser light sheet, estimated to be 100  $\mu\text{m}$  at a wavelength of 532 nm. More recently an innovative method for determining the three-dimensional location and velocity of particles was developed (Snoeyink and Wereley 2013). The wavefront from a particle is converted through a convex lens into a Bessel beam, the frequency and center of which can be directly related to the three-dimensional position of the particle.

In conclusion, one way forward would be to combine the thin laser sheet of classical and macro-PIV with telecentric lenses and fluorescent markers. Such a setup does not even need to be restricted to water environments, as Burgmann et al. (2011) were able to use fluorescent tracer particles to study small-scale wall-bounded gas flows. None of these ideas have been applied to, or tested in, sensory ecology. The study of flow sensing in organisms therefore has a bright future, but its students must be prepared to design their own tools, as off-the-shelf technology is generally unsuited to the models they study and the problems they face.

## Appendix

**Table 2.1** Summary of the different techniques, channel flow depth, and applications of micro-PIV from 20 papers on micro-PIV most pertinent to the scope of this review

Author	Year	Channel flow depth	Applications	Techniques	2D/3D	Velocity
Meinhart et al.	1999	30 $\mu\text{m}$	$\mu$ channel flow	NdYag laser	2D	
Cummings	2000	30 $\mu\text{m}$	Image processing	Argon ion Laser	2D	
Meinhart et al.	2000	90 $\mu\text{m}$	Inkjet print head	Nd YAG	2D	8 m/s
Kim et al.	2002	7 $\mu\text{m}$	$\mu$ channel, electroosmotic flow	Argon ion laser	2D	260 $\mu\text{m/s}$
Lee et al.	2002	690 $\mu\text{m}$	$\mu$ channel flow	Nd YAG laser	2D	
Devasenathipathy et al.	2003	50 $\mu\text{m}$	Electrokinetic flow		2D	
Devasenathipathy and Santiago	2003	107 $\mu\text{m}$	Silicon channel	Nd YAG laser	2D	20 mm/s
Meinhart and Wereley	2003	100 $\mu\text{m}$	AC electrokinetic flow	Mercury lamp	2D	110 $\mu\text{m/s}$
Sato et al.	2003					
Park et al.	2004					
Bitsch et al.	2005	30 $\mu\text{m}$	Blood flow in a capillary glass	LED	2D	4 mm/s
Liu et al.	2005	225 $\mu\text{m}$	Microcapillary flow	Nd YAG laser	2D	1 m/s
Boek et al.	2006	40 $\mu\text{m}$	Wormlike micellor fluid	Nd YAG laser	2D	4 mm/s
Bown et al.	2006	25 $\mu\text{m}$	DNA concentrator	Nd YAG laser	2D	5 $\mu\text{m/s}$
Curtin et al.	2006	233 $\mu\text{m}$	DNA, viscosity estimation	Nd YAG laser	2D	0.4 mm/s
Horiuchi et al.	2006	11 $\mu\text{m}$	$\mu$ channel, electroosmotic flow	Nd YAG laser	2D	100 $\mu\text{m/s}$
Kähler et al.	2006	Boundary layer of 5–7 mm	Wall-shear-stress and near-wall turbulence	Laser light sheet Nd: Yag laser	2D	5 m/s
Li and Olsen	2006	521 $\mu\text{m}$	Turbulent flow in $\mu$ channel	Nd YAG laser	2D	10 m/s
Lindken et al.	2006	200 $\mu\text{m}$	$\mu$ channel flow	NdYag laser, stereoscopy	3D	0.3 m/s
Mielnik and Saetran	2006	260 $\mu\text{m}$	Selective seeding	Sheet of seeding particles	2D	2 cm/s
Moghtaderi et al.	2006	300 $\mu\text{m}$	Baffle plate $\mu$ reactor	NdYag laser	2D	0.3 m/s
Sato and Hishida	2006					
Yan et al.	2006					

(continued)

**Table 2.1** (continued)

Author	Year	Channel flow depth	Applications	Techniques	2D/ 3D	Velocity
Yang and Chuang	2005					
Bown and Meinhart	2006	436 $\mu\text{m}$	$\mu$ channel	3D, stereoscopy	3D	16 $\mu\text{m/s}$
Lima et al.	2007	100 $\mu\text{m}$	Confocal $\mu\text{PIV}$	NdYag Laser	2D	0.6 mm/s
Natrajan et al.	2006					
Pereira et al.	2007					
Walsh et al.	2007					
Kim et al.	2008	70 $\mu\text{m}$	Mixing and pumping	Continuous laser	2D	15 $\mu\text{m/s}$
Lee et al.	2009	50 $\mu\text{m}$	Fluid mechanics of blood sucking	Continuous Nd:YAG laser	2D	0.4 cm/s
Mansoor and Stoeber	2010	200 $\mu\text{m}$	Drying of polymer solutions	HeNe laser	2D	1 $\mu\text{m/s}$
Raghavan et al.	2009					
Alharbi and Sick	2010	44 mm	Study of boundary layers in internal combustion engines	1 mm laser light sheet	2D	1.5 m/s
Nguyen et al.	2010	200 $\mu\text{m}$	Improvement of measurement	Continuous DPSS laser	2D	
Poelma et al.	2010	250 $\mu\text{m}$	Study of outflow tract of embryonic chicken heart	Scanning $\mu\text{PIV}$	3D	4 cm/s
Wereley and Meinhart	2010		Review of recent advances in $\mu\text{PIV}$	Confocal imaging, particle image defocusing, stereo imaging...	2D, 3D	
Kloosterman et al.	2010	148 $\mu\text{m}$	Increasing depth of correlation	Diode-pumped Nd:YLF laser	2D	
Patrick et al.	2010	150 $\mu\text{m}$	Hemodynamics	Bidirectional scanning micro PIV	2D	45 $\mu\text{m/s}$
Rossi et al.	2011	Theoretical work	Image preprocessing use of depth of correlation	Particle image defocusing		
Wang et al.	2010	300 $\mu\text{m}$	Pulsed micro-flows for insulin infusion therapy	Nd Yag laser	2D	30 mm/s
Cierpka et al.	2011	200 $\mu\text{m}$	Comparative analysis	Astigmatism- $\mu\text{PTV}$ , stereo- $\mu\text{PIV}$		75 mm/s
Eichler and Sattelmayer	2011	17.5 mm	Measurements of premixed flames	Long-distance micro-PIV	2D	

(continued)

**Table 2.1** (continued)

Author	Year	Channel flow depth	Applications	Techniques	2D/ 3D	Velocity
Jin and Yoo	2011	100–140 $\mu\text{m}$	Droplet merging	Continuous laser/ high speed camera	2D	4 cm/s
Nguyen et al.	2011	500 $\mu\text{m}$	Improvement of measurement	Volumetric-correlation PIV	3D	
Samarage et al.	2011	200 $\mu\text{m}$	Optimization of temporal averaging processes	Nd:Yag continuous laser	2D	
Sun et al.	2011	60 $\mu\text{m}$	Study of a microdiffuser	100 W Halogen lamp	2D	20 mm/s

**Table 2.2** Advantages and limitations of both standard macro-PIV and micro-PIV techniques according to seven criteria

	Macro PIV standard thin laser light sheet/non fluorescent particles	Micro PIV Volume illumination/fluorescent particles	Mixed technique: Telecentric lens/thin laser light sheet/ fluorescent particles
1. Glare and body surface reflexion	Standard illumination techniques lead to high reflection close to surfaces, and without fluorescent paint, there is a lack of information in the first 100 $\mu\text{m}$ of the boundary layer	The greatest advantage of the use of fluorescent particles: investigation of the flow in the 100 $\mu\text{m}$ closest to the receptor is possible	Use of fluorescent particles to reduce reflection of laser light close to the surface
2. Signal-to-noise ratio. Capacity of individual particle discrimination	The thin laser sheet thickness tends to reduce the background noise but the noise mainly depends on particle density: $C \ll \frac{1}{4Z} \left( \frac{M}{di} \right)^2$	The biggest problem with the technique when applied to biological flows and particularly 3D problems: the SNR increases with the increase of test section depth	Thin laser sheet to reduce undesirable background noise
3. Limit of magnification	Depends on lens magnification, but the upper limit with a standard binocular lens is 5 times, which represents a field of view of 2,000 $\mu\text{m}$	Theoretically there is no limit of magnification. Practically a 20 times magnification is sufficient for a large number of applications and represents a field of view of 440 $\mu\text{m}$	Telecentric lens allowing a 10 times magnification leading to a field of view of 880 $\mu\text{m}$
4. Diffraction of the particles	Diffraction effects and particle image size on CCD sensor are large due to the low numerical aperture ( $di = 15 \mu\text{m}$ )	The high numerical aperture of a microscopic lens (0.4) limits the diffraction ( $di = 3 \mu\text{m}$ )	Telecentric lens with a numerical aperture of 0.21 leading to an estimated diffraction of 6 $\mu\text{m}$

(continued)

**Table 2.2** (continued)

	Macro PIV standard thin laser light sheet/non fluorescent particles	Micro PIV Volume illumination/fluorescent particles	Mixed technique: Telecentric lens/thin laser light sheet/ fluorescent particles
5. Temporal resolution	At 5 times magnification and given the large SNR, real time and high frequency flow investigation is possible	To maintain a good SNR, the particle density needs to be low, and consequently often not high enough to provide good correlation or velocity fields without time averaging	High SNR expected even at high concentration, real time and high frequency possible
6. Working distance	Depends on lens but typically between 50 and 70 mm	The use of microscopic lens requires small working distances, generally a few mm. This constraint is hard to apply to the investigation of flows around 3D structures	Large working distance, allows the investigation of flows around 3D structures
7. Application fields (in the sensory ecological framework)	Steady and unsteady flows in air and water around 3D structures at a macro scale of a few millimeters	Steady flows in water around 2d structures at the scale of a few hundreds of microns (cells, protozoans, flows in vessels etc.)	The use of fluorescent particles constrains applications to steady and unsteady flows in water around 3D structures at a scale of a few hundreds of microns

The use of gray and white background colors respectively indicates for which criteria standard macro-PIV or micro-PIV perform better. The last column is for the new innovative mixed technique that exploits the advantages of both techniques

## References

- Adrian RJ, Westerweel J (2011) Particle image velocimetry. Cambridge University Press, Cambridge
- Alharbi AY, Sick V (2010) Investigation of boundary layers in internal combustion engines using a hybrid algorithm of high speed micro-PIV and PTV. *Exp Fluids* 49:949–959. doi:[10.1007/s00348-010-0870-8](https://doi.org/10.1007/s00348-010-0870-8)
- Barth FG, Wastl U, Humphrey JAC, Devarakonda R (1993) Dynamics of arthropod filiform hairs II Mechanical properties of spider trichobothria (*Cupiennius salei* Keys). *Philos Trans R Soc Lond B Biol Sci* 340:445–461
- Bathellier B, Steinmann T, Barth FG, Casas J (2012) Air motion sensing hairs of arthropods detect high frequencies at near-maximal mechanical efficiency. *J R Soc Interface* 9:1131–1143. doi:[10.1098/rsif-2011-0690](https://doi.org/10.1098/rsif-2011-0690)
- Bechert DW, Bruse M, Hage W (2000) Experiments with three-dimensional riblets as an idealized model of shark skin. *Exp Fluids* 28:403–412. doi:[10.1007/s003480050400](https://doi.org/10.1007/s003480050400)

- Bechert D, Bartenwerfer M (1989) The viscous flow on surfaces with longitudinal ribs. *J Fluid Mech* 206:105–129
- Bitsch L, Olesen LH, Westergaard CH, Bruus H, Klank H, Kutter JP (2005) Micro particle-image velocimetry of bead suspensions and blood flows. *Exp Fluids* 39:505–511
- Bleckmann H, Breithaupt T, Blickhan R, Tautz J (1991) The time course and frequency content of hydrodynamic events caused by moving fish, frogs, and crustaceans. *J Comp Physiol A* 168:749–757
- Blickhan R, Krick C, Zehren D, Nachtigall W (1992) Generation of a vortex chain in the wake of a subundulatory swimmer. *Naturwissenschaften* 79:220–221
- Boek ES, Padding JT, Anderson VJ, Briels WJ, Crawshaw JP (2006) Flow of entangled wormlike micellar fluids: mesoscopic simulations, rheology and  $\mu$ -PIV experiments. *J Non-Newton Fluid* 146:11–21
- Bown MR, Meinhart CD (2006) AC electroosmotic flow in a DNA concentrator. *Microfluid Nanofluid* 2:513–523. doi:[10.1007/s10404-006-0097-4](https://doi.org/10.1007/s10404-006-0097-4)
- Bown MR, MacInnes JM, RWK Allen (2006) Three-component micro-PIV using the continuity equation and a comparison of the performance with that of stereoscopic measurements. *Exp Fluids* 42:197–205. doi:[10.1007/s00348-006-0229-3](https://doi.org/10.1007/s00348-006-0229-3)
- Burgmann S, Van der Schoot N, Asbach C, Wartmann J, Lindken R (2011) Analysis of tracer particle characteristics for micro PIV in wall-bounded gas flows. *La Houille Blanche* 4:55–61. doi:[10.1051/lhb/2011041](https://doi.org/10.1051/lhb/2011041)
- Casas J, Dangles O (2010) Physical ecology of fluid flow sensing in arthropods. *Annu Rev Entomol* 55:505–520. doi:[10.1146/annurev-ento-112408-085342](https://doi.org/10.1146/annurev-ento-112408-085342)
- Casas J, Liu C, Krijnen G (2013) Biomimetic flow sensors encyclopedia. *Nanotechnology* 2013:264–276
- Casas J, Steinmann T, Dangles O (2008) The aerodynamic signature of running spiders. *PLoS ONE* 3:e2116. doi:[10.1371/journal.pone-0002116](https://doi.org/10.1371/journal.pone-0002116)
- Casas J, Steinmann T, Krijnen G (2010) Why do insects have such a high density of flow-sensing hairs? Insights from the hydromechanics of biomimetic MEMS sensors. *J R Soc Interface* 7:1487–1495. doi:[10.1098/rsif-2010-0093](https://doi.org/10.1098/rsif-2010-0093)
- Catton KB, Webster DR, Brown J, Yen J (2007) Quantitative analysis of tethered and free-swimming copepodid flow fields. *J Exp Biol* 210:299–310. doi:[10.1242/jeb-02633](https://doi.org/10.1242/jeb-02633)
- Chagnaud BP, Bleckmann H, Engelmann J (2006) Neural responses of goldfish lateral line afferents to vortex motions. *J Exp Biol* 209:327–342. doi:[10.1242/jeb-01982](https://doi.org/10.1242/jeb-01982)
- Cierpka C, Rossi M, Segura R, Mastrangelo F, Kähler CJ (2011) A comparative analysis of the uncertainty of astigmatism- $\mu$ PTV, stereo- $\mu$ PIV and  $\mu$ PIV. *Exp Fluids* 52:605–615. doi:[10.1007/s00348-011-1075-5](https://doi.org/10.1007/s00348-011-1075-5)
- Cummings EB (2000) An image processing and optimal nonlinear filtering technique for particle image velocimetry in microflows. *Exp Fluids* 29(1):S42–S50
- Curtin DM, Newport DT, Davies MR (2006) Utilising  $\mu$ -PIV and pressure measurements to determine the viscosity of a DNA solution in a microchannel. *Exp Therm Fluid Sci* 30:843–852
- Dangles O, Steinmann T, Pierre D, Vannier F, Casas J (2008) Relative contributions of organ shape and receptor arrangement to the design of cricket's cercal system. *J Comp Physiol A* 194:653–663. doi:[10.1007/s00359-008-0339-x](https://doi.org/10.1007/s00359-008-0339-x)
- Denissenko P, Lukashuk S, Breithaupt T (2007) The flow generated by an active olfactory system of the red swamp crayfish. *J Exp Biol* 210:4083–4091. doi:[10.1242/jeb-008664](https://doi.org/10.1242/jeb-008664)
- Devasenathipathy S, Santiago JG, Wereley ST, Meinhart CD, Takehara K (2003) Particle imaging techniques for microfabricated fluidic systems. *Exp Fluids* 34:504–514
- Devasenathipathy S, Santiago JG (2003) Electrokinetic flow diagnostics. In: Breuer K (ed) *Micro- and Nano-scale diagnostic techniques*. Springer, New York, pp 113–144
- Eichler C, Sattelmayer T (2011) Premixed flame flashback in wall boundary layers studied by long-distance micro-PIV. *Exp Fluids* 52:347–360. doi:[10.1007/s00348-011-1226-8](https://doi.org/10.1007/s00348-011-1226-8)
- Engelmann J, Hanke W, Bleckmann H (2002) Lateral line reception in still- and running water. *J Comp Physiol A* 188:513–526. doi:[10.1007/s00359-002-0326-6](https://doi.org/10.1007/s00359-002-0326-6)

- Fertin A, Casas J (2006) Efficiency of antlion trap construction. *J Exp Biol* 209:3510–3515. doi:[10.1242/jeb-02401](https://doi.org/10.1242/jeb-02401)
- Fertin A, Casas J (2007) Orientation towards prey in antlions: efficient use of wave propagation in sand. *J Exp Biol* 210:3337–3343. doi:[10.1242/jeb-004473](https://doi.org/10.1242/jeb-004473)
- García-Mayoral R, Jiménez J (2011) Drag reduction by riblets. *Philos T Roy Soc A* 369(1940):1412–1427. doi:[10.1098/rsta-2010-0359](https://doi.org/10.1098/rsta-2010-0359)
- Gnatzy W, Heusslein R (1986) Digger wasp against crickets: I receptors involved in the antipredator strategies of the prey. *Naturwissenschaften* 73:212–215
- Hanke W, Brücker C, Bleckmann H (2000) The ageing of the low-frequency water disturbances caused by swimming goldfish and its possible relevance to prey detection. *J Exp Biol* 203:1193–1200
- Hanke W, Wieskotten S, Niesterek B, Miersch L, Witte M, Brede M, Leder A et al (2012) Hydrodynamic perception in pinnipeds. *Note N Fl Mech Mul D* 119:255–270. doi:[10.1007/978-3-642-28302-4\\_16](https://doi.org/10.1007/978-3-642-28302-4_16)
- Horiuchi K, Dutta P, Richards CD (2006) Experiment and simulation of mixed flows in a trapezoidal microchannel. *Microfluid Nanofluid* 3:347–358. doi:[10.1007/s10404-006-0129-0](https://doi.org/10.1007/s10404-006-0129-0)
- Humphrey JAC, Devarakonda R, Iglesias I, Barth FG (1993) Dynamics of arthropod filiform hairs: I mathematical modelling of the hair and air motions. *Philos Trans R Soc Lond B Biol Sci* 340:423–440
- Inoué S, Spring KR (1997) Video microscopy. Plenum, Oxford
- Jacobs GA, Miller JP, Aldworth Z (2008) Computational mechanisms of mechanosensory processing in the cricket. *J Exp Biol* 211:1819–1828. doi:[10.1242/jeb-016402](https://doi.org/10.1242/jeb-016402)
- Jin BJ, Yoo JY (2011) Visualization of droplet merging in microchannels using micro-PIV. *Exp Fluids* 52:235–245. doi:[10.1007/s00348-011-1221-0](https://doi.org/10.1007/s00348-011-1221-0)
- Kähler CJ, Scharnowski S, Cierpka C (2012) On the uncertainty of digital PIV and PTV near walls. *Exp Fluids* 52:1641–1656. doi:[10.1007/s00348-012-1307-3](https://doi.org/10.1007/s00348-012-1307-3)
- Kähler CJ, Scholz U, Ortmanns J (2006) Wall-shear-stress and near-wall turbulence measurements up to single pixel resolution by means of long-distance micro-PIV. *Exp Fluids* 41:327–341. doi:[10.1007/s00348-006-0167-0](https://doi.org/10.1007/s00348-006-0167-0)
- Kämper G, Kleindienst HU (1990) Oscillation of cricket sensory hairs in a low-frequency sound field. *J Comp Physiol A* 167:193–200
- Kim MJ, Beskok A, Kihm KD (2002) Electro-osmosis-driven micro-channel flows: A comparative study of microscopic particle image velocimetry measurements and numerical simulations. *Exp Fluids* 33:170–180
- Kim BJ, Yoon SY, Lee KH, Sung HJ (2008) Development of a microfluidic device for simultaneous mixing and pumping. *Exp Fluids* 46:85–95. doi:[10.1007/s00348-008-0541-1](https://doi.org/10.1007/s00348-008-0541-1)
- Kloosterman A, Poelma C, Westerweel J (2010) Flow rate estimation in large depth-of-field micro-PIV. *Exp Fluids* 50:1587–1599. doi:[10.1007/s00348-010-1015-9](https://doi.org/10.1007/s00348-010-1015-9)
- Klopsch C, Kuhlmann HC, Barth FG (2012) Airflow elicits a spider's jump towards airborne prey I Airflow around a flying blowfly. *J R Soc Interface* 9:2591–2602. doi:[10.1098/rsif-2012-0186](https://doi.org/10.1098/rsif-2012-0186)
- Koehl MAR (2004) Biomechanics of microscopic appendages: functional shifts caused by changes in speed. *J Biomech* 37:789–795. doi:[10.1016/j.jbiomech-2003-06-001](https://doi.org/10.1016/j.jbiomech-2003-06-001)
- Krijnen G, Dijkstra M, van Baar J, Shankar S, Kuipers W, de Boer J, Altpeter D, Lammerink T, Wiegink R (2006) MEMS based hair flow-sensors as model systems for acoustic perception studies. *Nanotechnology* 17:84–89. doi:[10.1088/0957-4484/17/4/013](https://doi.org/10.1088/0957-4484/17/4/013)
- Kumagai T, Shimozawa T, Baba Y (1998) The shape of windreceptor hairs of cricket and cockroach. *J Comp Physiol A* 183:187–192
- Landolf G, Jacobs MA (1995) Direction sensitivity of the filiform hair population of the cricket cercal system. *J Comp Physiol A* 177:759–766
- Lee SY, Wereley ST, Gui L, Qu W, Mudawar I (2002) Microchannel flow measurement using micro Particle Image Velocimetry. In: Proceedings of IMECE2002 ASME international mechanical engineering congress and exposition. New Orleans, Louisiana, 17–22 Nov 2002



- Lee SJ, Kim BH, Lee JY (2009) Experimental study on the fluid mechanics of blood sucking in the proboscis of a female mosquito. *J Biomech* 42:857–864. doi:[10.1016/j.jbiomech-2009-01-039](https://doi.org/10.1016/j.jbiomech-2009-01-039)
- Lee SJ, Lee SH (2001) Flow field analysis of a turbulent boundary layer over a riblet surface. *Exp Fluids* 30:153–166. doi:[10.1007/s003480000150](https://doi.org/10.1007/s003480000150)
- Li H, Olsen MG (2006) Micro PIV measurements of turbulent flow in square microchannels with hydraulic diameters from 200  $\mu\text{m}$  to 640  $\mu\text{m}$ . *Int J Heat Fluid Flow* 27:123–134. doi:[10.1016/j.ijheatfluidflow-2005-02-003](https://doi.org/10.1016/j.ijheatfluidflow-2005-02-003)
- Lima R, Wada S, Takeda M, Tsubota K, Yamaguchi T (2007) In vitro confocal micro-PIV measurements of blood flow in a square microchannel: the effect of the haematocrit on instantaneous velocity profiles. *J Biomech* 40:2752–2757. doi:[10.1016/j.jbiomech-2007-01-012](https://doi.org/10.1016/j.jbiomech-2007-01-012)
- Lindken R, Westerweel J, Wieneke B (2006) Stereoscopic micro particle image velocimetry. *Exp Fluids* 41:161–171. doi:[10.1007/s00348-006-0154-5](https://doi.org/10.1007/s00348-006-0154-5)
- Liu D, Garimella SV, Wereley ST (2005) Infrared micro-particle image velocimetry in silicon-based microdevices. *Exp Fluids* 38:385–392
- Magal C, Dangles O, Caparroy P, Casas J (2006) Hair canopy of cricket sensory system tuned to predator signals. *J Theor Biol* 241:459–466. doi:[10.1016/j.jtbi-2005-12-009](https://doi.org/10.1016/j.jtbi-2005-12-009)
- Mansoor I, Stoeber B (2010) PIV measurements of flow in drying polymer solutions during solvent casting. *Exp Fluids* 50:1409–1420. doi:[10.1007/s00348-010-1000-3](https://doi.org/10.1007/s00348-010-1000-3)
- McHenry MJ, Strother JA, van Netten SM (2008) Mechanical filtering by the boundary layer and fluid-structure interaction in the superficial neuromast of the fish lateral line system. *J Comp Physiol A* 194:795–810. doi:[10.1007/s00359-008-0350-2](https://doi.org/10.1007/s00359-008-0350-2)
- Mead KS (2003) Fine-scale patterns of odor encounter by the antennules of mantis shrimp tracking turbulent plumes in wave-affected and unidirectional flow. *J Exp Biol* 206:181–193. doi:[10.1242/jeb-00063](https://doi.org/10.1242/jeb-00063)
- Meinhart CD, Wereley ST, Gray MHB (2000) Volume illumination for two-dimensional particle image velocimetry. *Meas Sci Technol* 11:809–814
- Meinhart CD, Wereley ST (2003) The theory of diffraction-limited resolution in microparticle image velocimetry. *Meas Sci Technol* 14:1047–1053
- Meinhart CD, Wereley ST, Santiago JG (1999) PIV measurements of a microchannel flow. *Exp Fluids* 27:414–419
- Mielnik MM (2003) Micro-PIV and its application to some BioMEMS related microfluidic flows. PHD Thesis. ISBN 82-471-6954-1
- Mielnik MM, Saetran LR (2006) Selective seeding for micro-PIV. *Exp Fluids* 41(155–159):1007. doi:[10/s00348-005-0103-8](https://doi.org/10/s00348-005-0103-8)
- Miller JP, Krueger S, Heys JJ, Gedeon T (2011) Quantitative characterization of the filiform mechanosensory hair array on the cricket cercus. *PLoS ONE* 6(11):e27873. doi:[10.1371/journal.pone-0027873](https://doi.org/10.1371/journal.pone-0027873)
- Moghtaderi B, Shames I, Djenidi L (2006) Microfluidic characteristics of a multi-holed baffle plate micro-reactor. *Int J Heat Fluid Fl* 27:1069–1077. doi:[10.1016/j.ijheatfluidflow-2006-01-008](https://doi.org/10.1016/j.ijheatfluidflow-2006-01-008)
- Morley EL, Steinmann T, Casas J, Robert D (2012) Directional cues in *Drosophila melanogaster* audition: structure of acoustic flow and inter-antennal velocity differences. *J Exp Biol* 215:2405–2413. doi:[10.1242/jeb-068940](https://doi.org/10.1242/jeb-068940)
- Müller U, Heuvel B, Stamhuis E, Videler J (1997) Fish foot prints: morphology and energetics of the wake behind a continuously swimming mullet (*Chelon labrosus* Risso). *J Exp Biol* 200:2893–2906
- Natrajan VK, Yamaguchi E, Christensen KT (2006) Statistical and structural similarities between micro and macroscale wall turbulence. *Microfluid Nanofluid* 3:89–100. doi:[10.1007/s10404-006-0105-8](https://doi.org/10.1007/s10404-006-0105-8)
- Nguyen CV, Carberry J, Fouras A (2011) Volumetric-correlation PIV to measure particle concentration and velocity of microflows. *Exp Fluids* 52:663–677. doi:[10.1007/s00348-011-1087-1](https://doi.org/10.1007/s00348-011-1087-1)

- Nguyen CV, Fouras A, Carberry J (2010) Improvement of measurement accuracy in micro PIV by image overlapping. *Exp Fluids* 49:701–712. doi:[10.1007/s00348-010-0837-9](https://doi.org/10.1007/s00348-010-0837-9)
- Park J, Choi C, Kihm K (2004) Optically sliced micro-PIV using confocal laser scanning microscopy (CLSM). *Exp Fluids* 37:105–119. doi:[10.1007/s00348-004-0790-6](https://doi.org/10.1007/s00348-004-0790-6)
- Patrick MJ, Chen CY, Frakes DH, Dur O, Pekkan K (2010) Cellular-level near-wall unsteadiness of high-hematocrit erythrocyte flow using confocal  $\mu$ PIV. *Exp Fluids* 50:887–904. doi:[10.1007/s00348-010-0943-8](https://doi.org/10.1007/s00348-010-0943-8)
- Pereira F, Lu J, Castaño-Graff E, Gharib M (2007) Microscale 3D flow mapping with  $\mu$ DDPIV. *Exp Fluids* 42:589–599. doi:[10.1007/s00348-007-0267-5](https://doi.org/10.1007/s00348-007-0267-5)
- Poelma C, Van der Heiden K, Hierck BP, Poelmann RE, Westerweel J (2010) Measurements of the wall shear stress distribution in the outflow tract of an embryonic chicken heart. *J R Soc Interface* 7:91–103. doi:[10.1098/rsif-2009-0063](https://doi.org/10.1098/rsif-2009-0063)
- Raffel M, Willert K, Kompenhans J (1998) Particle image velocimetry, a practical guide. Springer, Berlin
- Raghavan RV, Friend JR, Yeo LY (2009) Particle concentration via acoustically driven microcentrifugation: microPIV flow visualization and numerical modelling studies. *Microfluidic Nanofluidic* 8:73–84. doi:[10.1007/s10404-009-0452-3](https://doi.org/10.1007/s10404-009-0452-3)
- Reidenbach MA, George N, Koehl MAR (2008) Antennule morphology and flicking kinematics facilitate odor sampling by the spiny lobster, *Panulirus argus*. *J Exp Biol* 211:2849–2858. doi:[10.1242/jeb-016394](https://doi.org/10.1242/jeb-016394)
- Rossi M, Segura R, Cierpka C, Kähler CJ (2011) On the effect of particle image intensity and image preprocessing on the depth of correlation in micro-PIV. *Exp Fluids* 52(4):1063–1075. doi:[10.1007/s00348-011-1194-z](https://doi.org/10.1007/s00348-011-1194-z)
- Samarage CR, Carberry J, Hourigan K, Fouras A (2011) Optimisation of temporal averaging processes in PIV. *Exp Fluids* 52:617–631. doi:[10.1007/s00348-011-1080-8](https://doi.org/10.1007/s00348-011-1080-8)
- Santiago JG, Wereley ST, Meinhart CD, Beebe DJ, Adrian RJ (1998) A particle image velocimetry system for microfluidics. *Exp Fluids* 25:316–319. doi:[10.1007/s003480050235](https://doi.org/10.1007/s003480050235)
- Sato Y, Hishida K (2006) Electrokinetic effects on motion of submicron particles in microchannel. *Fluid Dyn Res* 38:787–802. doi:[10.1016/j-fluiddyn-2006-04-003](https://doi.org/10.1016/j-fluiddyn-2006-04-003)
- Sato Y, Inaba S, Hishida K, Maeda M (2003) Spatially averaged time-resolved particle-tracking velocimetry in microspace considering Brownian motion of submicron fluorescent particles. *Exp Fluids* 35:167–177. doi:[10.1007/s00348-003-0643-8](https://doi.org/10.1007/s00348-003-0643-8)
- Shimozawa T, Kanou M (1984) The aerodynamics and sensory physiology of range fractionation in the cercal filiform sensilla of the cricket *Gryllus bimaculatus*. *J Comp Physiol A* 155:495–505
- Shimozawa T, Kumagai T, Baba Y (1998) Structural scaling and functional design of the cercal wind-receptor hairs of cricket. *J Comp Physiol A* 183:171–186
- Shimozawa T, Murakami J, Kumagai T (2003) Cricket wind receptors: thermal noise for the highest sensitivity known. In: Barth FB, Humphrey JAC, Secomb T (eds) *Sensors and sensing in biology and engineering*. Springer, Berlin, pp 145–157
- Snoeyink C, Wereley S (2013) A novel 3D3C particle tracking method suitable for microfluidic flow measurements. *Exp Fluids* 54:1453. doi:[10.1007/s00348-012-1453-7](https://doi.org/10.1007/s00348-012-1453-7)
- Stamhuis EJ, Videler JJ, Duren LAV, Mu UK (2002) Applying digital particle image velocimetry to animal-generated flows: traps, hurdles and cures in mapping steady and unsteady flows in Re regimes between 10–2 and 105. *Exp Fluids* 33:801–813. doi:[10.1007/s00348-002-0520-x](https://doi.org/10.1007/s00348-002-0520-x)
- Steinmann T, Casas J, Krijnen G, Dangles O (2006) Air-flow sensitive hairs: boundary layers in oscillatory flows around arthropod appendages. *J Exp Biol* 209:4398–4408. doi:[10.1242/jeb-02506](https://doi.org/10.1242/jeb-02506)
- Sterbing-D'Angelo S, Chadha M, Chiu C, Falk B, Xian W, Barcelo J, Zook JM et al (2011) Bat wing sensors support flight control. *PNAS* 108:11291–11296. doi:[10.1073/pnas-1018740108](https://doi.org/10.1073/pnas-1018740108)
- Sun C, Lee HC, Kao RX (2011) Diagnosis of oscillating pressure-driven flow in a microdiffuser using micro-PIV. *Exp Fluids* 52:23–35. doi:[10.1007/s00348-011-1204-1](https://doi.org/10.1007/s00348-011-1204-1)
- Tautz J, Markl H (1979) Caterpillars detect flying wasps by hairs sensitive to airborne vibration. *Behav Ecol Sociobiol* 4:101–110

- Walsh PA, Walsh EJ, Davies MRD (2007) On the out-of-plane divergence of streamtubes in planar mini-scale flow focusing devices. *Int J Heat Fluid Fl* 28:44–53. doi:[10.1016/j.ijheatfluidflow-2006-05-006](https://doi.org/10.1016/j.ijheatfluidflow-2006-05-006)
- Wang B, Demuren A, Gyuricsko E, Hu H (2010) An experimental study of pulsed micro-flows pertinent to continuous subcutaneous insulin infusion therapy. *Exp Fluids* 51:65–74. doi:[10.1007/s00348-010-1033-7](https://doi.org/10.1007/s00348-010-1033-7)
- Wereley ST, Meinhart CD (2010) Recent advances in micro-particle image velocimetry. *Annu Rev Fluid Mech* 42:557–576. doi:[10.1146/annurev-fluid-121108-145427](https://doi.org/10.1146/annurev-fluid-121108-145427)
- Windsor SP, Norris SE, Cameron SM, Mallinson GD, Montgomery JC (2010a) The flow fields involved in hydrodynamic imaging by blind Mexican cave fish (*Astyanax fasciatus*) Part I: open water and heading towards a wall. *J Exp Biol* 213:3819–3831. doi:[10.1242/jeb-040741](https://doi.org/10.1242/jeb-040741)
- Windsor SP, Norris SE, Cameron SM, Mallinson GD, Montgomery JC (2010b) The flow fields involved in hydrodynamic imaging by blind Mexican cave fish (*Astyanax fasciatus*), Part II: gliding parallel to a wall. *J Exp Biol* 213:3832–3842. doi:[10.1242/jeb-040790](https://doi.org/10.1242/jeb-040790)
- Yan DG, Yang C, Huang XY (2006) Effect of finite reservoir size on electroosmotic flow in microchannels. *Microfluid Nanofluid* 3:333–340. doi:[10.1007/s10404-006-0135-2](https://doi.org/10.1007/s10404-006-0135-2)
- Yang CT, Chuang HS (2005) Measurement of a microchamber flow by using a hybrid multiplexing holographic velocimetry. *Exp Fluids* 39:385–396. doi:[10.1007/s00348-005-1022-4](https://doi.org/10.1007/s00348-005-1022-4)

Flow Sensing in Air and Water

Behavioral, Neural and Engineering Principles of  
Operation

Bleckmann, H.; Mogdans, J.; Coombs, S.L. (Eds.)

2014, XIII, 562 p. 200 illus., 77 illus. in color., Hardcover

ISBN: 978-3-642-41445-9